SCANNING ELECTRON MICROANALYSIS AND ANALYTICAL CHALLENGES OF MAPPING ELEMENTS IN URBAN ATMOSPHERIC PARTICLES

Joseph M. Conny*
Surface and Microanalysis Science Division
National Institute of Standards and Technology
Gaithersburg, MD 20899

Gary A. Norris
National Exposure Research Laboratory
U.S. Environmental Protection Agency
Research Triangle Park, NC 27711

* Author to whom correspondence should be sent.

Keywords: atmospheric aerosol, particulate matter, SEM, energy-dispersive x-ray spectroscopy, elemental mapping, particle heterogeneity

ABSTRACT

Elemental mapping with energy-dispersive x-ray spectroscopy (EDX) associated with scanning electron microscopy is highly useful for studying internally-mixed atmospheric particles. Presented is a study of individual particles from urban airsheds and the analytical challenges in qualitatively determining the composition and origin of heterogeneous urban-air particles from high-resolution elemental maps. Coarse-mode particles were taken from samples collected in three U.S. cities: Atlanta, Los Angeles, and Seattle. Elemental maps distinguished particles with heterogeneously-mixed phases from those with homogeneously-mixed phases that also contained inclusions or surface adducts. Elemental mapping at low and high beam energies, along with imaging at an oblique angle helped to classify particles by origin. The impact of particle shape on x-ray microanalysis was demonstrated by having the beam enter the particle at $\geq 52°$ from normal. Potential misinterpretations of particle composition due to artifacts in the elemental maps were minimized by tilt imaging to reveal particle surface roughness and depth, mapping at low beam energies, noting the position of the EDX detector in the map field, and assessing differences in the mass absorption coefficients of the particle's major elements to anticipate x-ray self-absorption.

1. INTRODUCTION

Presented here is a qualitative scanning electron microscopy (SEM) and x-ray microanalysis study showing the morphological and compositional variations of coarse atmospheric particles (2.5 μm to 10 μm) from urban areas. The principal objective is to demonstrate the analytical challenges in interpreting the composition and origin of urban particles from high-definition elemental maps of individual particles based on energy-dispersive x-ray (EDX) microanalysis.

High-definition compositional mapping is essential for determining the heterogeneity of individual atmospheric particles. Composition and heterogeneity are critical factors in understanding the radiative impact of aerosols and their role in climate change (*1-3*). Radiative transfer models have demonstrated that the placement of chemically-distinct substructures in particles greatly affects their light scattering and absorption properties (*4-6*). Compositional heterogeneity may also be an important factor in how aerosols affect health. For example, pulmonary health may be adversely affected when coarse particles deposited in the lung contain a distinctive surface phase that readily dissolves. While automated SEM is often used for characterizing populations of atmospheric particles in a sample, the technique does not provide high-resolution maps of each particle. Elemental mapping is often essential for providing follow-up confirmation of aerosol source types in samples analyzed by automated SEM. Thus, mapping is highly useful for informing other types of analyses.

When elemental mapping is employed in aerosol studies, often a field of particles is mapped at lower magnification rather than individual particles at high magnification. In this case, the

resolution is often so limited that the ability to discern the heterogeneity of individual particle is lacking. As a result, potential analytical difficulties in acquiring accurate maps of individual particles may not be fully appreciated. There may be little interest in considering mapping artifacts and employing additional measures to avoid them. Here, we show how high-resolution EDX mapping of individual heterogeneous particles is affected by the complexity in the spatial distribution of elemental phases as well as particle surface roughness. We also show the benefit of imaging atmospheric particles at an oblique angle to assess particle height, which helps in choosing an appropriate electron-beam energy for x-ray microanalysis and in interpreting EDX maps with potential analytical artifacts.

Scanning electron microscopy (SEM) for analyzing ambient air particles has been applied in a number of studies involving the urban airshed and in comparisons between urban and rural airsheds (*7-9*). A number of studies have characterized various regional emission sources and airsheds (*10-13*). As in continental non-urban air, urban air contains natural coarse particles associated with wind-blown releases from exposed crustal surfaces, biogenic releases (e.g., viruses, bacteria, pollen, spores, animal, and plant tissue), and volcanic eruptions. We might also expect large amounts of mineral dust in urban air due to road wear and construction site preparation since human activities may account for 20 % to 50 % of the mineral dust in the global atmosphere (*14,15*). However, we might also expect coarse particles of uniquely anthropogenic origin in urban air such as metal corrosion, cement and masonry wear, tire wear, demolition dust, emissions from energy-intensive manufacturing, etc. Determining the origin of atmospheric particles from natural sources is benefitted by the wealth of mineralogical

information available. However, mineralogy may offer limited insight into the origin of urban particles.

In quantitative x-ray microanalysis with SEM, a specimen is typically assumed to have a smooth flat surface, within the range of the beam electrons, from which photons at the surface radiate with unrestricted trajectories toward the detector (*16*). Atmospheric particles typically have surface roughness, so the assumption of a smooth flat surface is often invalid, and quantitative particle analysis is problematic. Measurement accuracy for flat, polished specimens is around 2 % of the actual mass for major elements. However, accuracy for particles is typically several-fold larger: 10 % to 20 % of the actual mass (*17*). Qualitative high-resolution elemental mapping of particles is problematic for the same reason. If surface roughness is such that photons emerging from one part of the particle are absorbed by another part of the particle, then an artifact will appear in the map as a region deficient in the element generating the photons. The problem is compounded when the spatial distributions of chemical phases are inhomogeneous.

The effect of particle surface roughness on x-ray microanalysis must be understood with awareness of the position of the EDX detector in the map field and the differences in mass absorption coefficients for x-ray photons of the detected elements. The importance of assessing detector position and mass absorption coefficients is demonstrated in *Supporting Information*. Because the detector has a fixed position, maps of an inhomogeneous particle taken at different rotations of the stage may result in substantial differences in the spatial distribution of the chemical phases (Fig. S1).

2. EXPERIMENTAL

Rather than an exhaustive microanalysis of particulate matter, we studied a small number of coarse-mode particles from samples collected in three geographically-distinct U.S. cities. Five particles were selected from each of filter samples collected in Atlanta during summer 2004, Los Angeles sample during fall 2004, and Seattle sample during winter 2004-2005. Particles were selected to provide a range of morphological and compositional complexities, based on the spatial distribution of chemical phases. To prepare specimens for microanalysis, particles on small sections of the filters were migrated to polished 5 mm x 5 mm silicon wafer squares in a microcentrifuge. Further details about filter sampling and specimen preparation are in *Supporting Information.*

Electron imaging and x-ray microanalysis were performed with an FEI Nova NanoLab 600 DualBeam instrument. [(Commercial products identified here specify the means by which experiments were conducted. Such identification is not intended to imply recommendation or endorsement by NIST or USEPA nor that the indentified products are necessarily the best available for the purpose.)] Secondary electron images were collected with the electron beam at 15 keV and 0.14 nA unless otherwise noted. Tilted images were taken with the beam at 52°, 55° or 60° from the normal. Particle height was determined by measuring the particle's y-dimension in the tilt image and correcting for image foreshortening caused by imaging at an angle above the substrate horizontal.

disclaimer

Elemental mapping was performed at either 20 keV and 2.4 nA, 15 keV and 0.58 nA, 10 keV and 0.54 nA, 5 keV and 0.40 nA, or 4 keV and 0.34 nA with an Oxford Si(Li) detector. Maps were created in most cases from 1000 scan frames using a dwell time of 100 μs and 128x112-pixel resolution. Spatial resolution of the maps varied from 14 nm to 278 nm, with 86 % of the maps having a spatial resolution less than 103 nm. For all maps, the position of the EDX detector is in the upper right corner of the map field. Further details about the FEI DualBeam instrument and the correction for image foreshortening are in *Supporting Information*.

Two to three phases in the same map are shown by assigning false colors to elements from the red/green/blue additive color model. The purpose is show the spatial arrangement of elements and their combinations as yellow (red+green), cyan (green+blue), and purple (red+blue). Gray-scale is used when only one element is presented.

3. RESULTS AND DISCUSSION

3.1. Atlanta Particles

Figure 1 show electron images and elemental maps of five selected particles (A1 to A4) from Atlanta that we've attempted to identify as natural or anthropogenic. Particle A1 (Fig. 1a) is both compositionally and structurally complex. The particle is spatially homogeneous in some elements and inhomogeneous in others. Carbon in *m1*, likely as carbonate due to the corresponding presence of oxygen (*m2*), appears concentrated toward the top of the particle. Carbon density is greatest nearer the EDX detector (upper right corner of map). In this case, the lack of carbon in the lower part of *m1* is likely an artifact due to x-ray absorption. Like carbon, principal metals iron (*m3*) and aluminum (*m4*) are also homogeneously-distributed. Semi-quantitative analysis of the particle (Fig. S3 in *Supplemental Information*) showed 49 % more aluminum than iron. Calcium with sulfur, sodium, and titanium are in discrete locations and represent inhomogeneously-distributed phases. The calcium/sulfur inclusions are consistent with gypsum ($CaSO_4 \cdot 2H_2O$).

Compositional complexity is believed to be more likely in particles of mineral origin (*18-20*) than in particles of biological or anthropogenic origin. Thus, we might expect A1 to be of mineral origin. However, a significant exception could be anthropogenic emissions from the byproducts of ore processing in smelters. Thus, we cannot rule out the particle as an industrial byproduct or, perhaps, an ore processing byproduct used in concrete. An aluminum smelter is known to operate 60 miles northwest of Atlanta (Station Source Permitting Program, Georgia Air

Protection Branch, Georgia Dept. of Natural Resources). With the 5 keV beam and the fact that the particle appears to have sufficient depth (nominally 5.5 μm) to confine the lower-energy electrons, it appears from map (*m4*) that little or no silicon is present in the particle. Since metal-containing minerals are commonly silicates, the fact that little evidence of silicon exists supports the argument that the particle is an industrial byproduct.

Particles A2 and A3 (Fig. 1b and c) are also consistent with particles of anthropogenic origin. Particle A2 is nearly pure carbon as indicated by map *m1*. The particle's conchoidal fracture surface, shape, and composition, makes it consistent with crushed, relatively non-porous, coke (*21*); however we cannot rule out tire wear. The smaller surface particles are oxides of aluminum and iron. Map *m2* reveals sulfur associated with the main particle. With a mass absorption coefficient of 50415 $cm^2\ g^{-1}$(*22*), sulfur is a very strong absorber of carbon x-rays, while carbon is a weak absorber of sulfur x-rays (192 $cm^2\ g^{-1}$). The relative strength and weakness of the carbon and sulfur signals, respectively, indicate that sulfur is a minor constituent within the particle or on its surface. As a surface phase, we might expect sulfate oxygen from oxidation of atmospheric SO_2. Since no oxygen is associated with the main particle, sulfur is likely within the particle, perhaps from sulfur cross linkages in tire rubber.

Particle A3 (Fig. 1c) is roughly spherical particle (particle depth 5.78 μm) and is compositionally homogenous in several elements, including carbon, chlorine, calcium, and copper (maps *m1-m4*, respectively). Also included in the EDX spectrum (Fig. S4 in *Supporting Information*) was nitrogen. Images of the particle at 20 keV and 5 keV are vastly different because only lower-energy imaging reveals the particle's surface porosity. The presence of carbon, copper, and

nitrogen, in particular, suggest that particle is a phthalocyanine-based. The presence of chlorine also suggests a phthalocyanine green pigment. The particle's homogeneous composition and its shape suggest that it was formed as a well-mixed pigment droplet.

The maps and the spectrum (*Supporting Information* Fig. S4b) reveal that carbon exhibits much higher intensity than oxygen. In this case, it is unlikely that the disparity in intensities is due to absorption of oxygen x-rays alone. While calcium has a large mass absorption coefficient for oxygen x-rays (22561 $cm^2\ g^{-1}$), copper has a fairly large mass absorption coefficient for carbon x-rays (19140 $cm^2\ g^{-1}$) (*22*). The presence of oxygen and calcium suggests that some of the carbon may be in form of calcium carbonate which serves as a paint extender.

The Atlanta sample contained a relatively large number of particles that were decidedly biogenic based on unique particle architectures and symmetries. For A4 (Fig. 1d), the main particle is carbonaceous but without oxygen, which rules out non-biogenic carbonate. Here, key evidence of the particle's biogenicity is the presence of brochosomes (arrows) from leafhopper insects (*23*). Two apparently non-biogenic surface adducts are also present. The image and 5 keV maps *m1* and *m2* reveal an aluminum oxide adduct in the low left corner of the particle and a calcium and sulfur adduct at the center. In this case, the particle appears to have lost some of its biogenic identity, perhaps picking up the non-carbonaceous adducts in transit. The 15 keV map (*m3*) shows that with a more energetic beam, which leaves fewer electrons in the particle to generate x-rays, the adducts are less detectable and easily overlooked. An additional biogenic particle, A5 shown in *Supporting Information* Fig. S5a, is an example where the tilt image specifically provides key evidence of its biogenicity.

3.2. Los Angeles Particles

Figure 2 shows electron images and elemental maps of selected particles from Los Angeles. Particle LA1 (Fig. 2a) resembles the Atlanta A1 particle in that it is compositionally rich with both homogeneously- and inhomogeneously-distributed elements. In addition to carbon, several metals are present including calcium, iron, sodium, magnesium, and aluminum. In *m1* and *m2*, calcium and magnesium are distributed homogeneously. The spatial correlation of these elements with carbon and oxygen makes the particle consistent with dolomite ($CaMg(CO_3)$). Aluminum and iron occupy distinctly separate phases. Since dolomite is often used as an aggregate in concrete, it is plausible that the particle is concrete wear, with the aluminum and iron phases from tricalcium aluminate and/or tetracalcium aluminoferrite, which are common additives in Portland cement (*24*).

LA1 is an example of the effect on mapping from widely-varying mass absorption coefficients. The normal image *i1* and tilted image *i2* indicate that x-rays from the peripheral iron grain on the left side of the particle (arrow) do not have a clear path to the EDX detector. Yet, the iron signal is strong in *m1* while the carbon and oxygen signals are weak in the lower left corner of *m3*. The iron signal is strong because homogenously-distributed carbon, oxygen, and magnesium, with mass absorption coefficients of 8.7 $cm^2\ g^{-1}$, 22 $cm^2\ g^{-1}$, and 78 $cm^2\ g^{-1}$, respectively, absorb Fe *Kα* x-rays weakly. In contrast, the carbon and oxygen are relatively weak because calcium is a moderately strong absorber of carbon (coefficient 6520 $cm^2\ g^{-1}$), but a strong absorber of oxygen (coefficient 22561 $cm^2\ g^{-1}$) (*22*).

LA2 (Fig. 2b) is a thin iron oxide particle (oxygen map not shown) associated with soot. As a combination of rust and soot, the particle is likely vehicular dust such as engine or tailpipe rust. It is shown here as a coarse particle because its major axis well exceeds 2.5 μm. However, based on the angled image (*i2*) in Fig. 5b, the particle's thinness likely caused it to behave as a fine particle aerodynamically, and therefore, it is plausible the particle coalesced with soot while suspended in the atmosphere.

Particle LA3 (Fig. 2c) is crystalline-like with oxides of sodium, magnesium, and calcium and likely contains carbonate as well. The tilted SEM image (*i2*) reveals details of its architecture, the pitched surface topography and a major fracture within the particle. The particle's nominal height is 3.3 μm. While the particle may look perhaps like a glass fragment, the lack of silicon in the particle at 5 keV (map *m2*) suggests that particle is a carbonate mineral.

For Particle LA4 (Fig. 2d), its rounded shape and the fusing of the large calcium phase with the main particle suggests that the particle was formed at high temperature. The particle clearly contains no silicon. The particle contains carbon but is not a carbonate because oxygen is not assocated with the carbon phase. (The carbon and oxygen maps, along with sulfur, are shown in *Supporting Information* Fig. S6.) In fact, the particle resembles coke derived from petroleum (*21*). However, the particle has barium inclusions, and barium has been associated with brake abrasion (*25*), which also occurs at elevated temperature. Thus, given the particle's composition and the proximity of the sampling site to a major freeway, the particle may be vehicle brake wear.

Particle LA5 (Fig. 2e) contains homogeneously-mixed phases of potassium, calcium, iron, copper, and titanium with oxygen and sulfur. However, the Fig. 2e map shows that numerous grains of zirconium are also present, and thus, the particle exhibits some inhomogeneity. (Additional maps are shown in *Supporting Information* Fig.. S7). The absence of significant silicon (*m2*) with zirconium in the particle suggests that it is not a natural mineral dust such as zircon ($ZrSiO_4$). Rather, the type of transition metals present, particularly copper in combination with zirconium, suggests that the particle is derived from an industrially-produced alloy or ceramic.

3.3. Seattle Particles

Particles selected from the Seattle sample (Fig. 3) further show the diversity of coarse particles from urban areas. Particles S1 to S3 are likely of mineral origin. Particle S1 (Fig. 3a) is unique here because it is a package of adducts and, thus, represents a particle with only inhomogeneously-distributed phases. Maps *m1* and *m2* suggest the presence of silicates, one of which is possibly $NaAlSi_3O_8$, the common feldspar albite, as indicated by the coincidence with sodium and aluminum in maps *m3* and *m4*. Nevertheless, mapping at a lower energy would have benefitted the assessment. The presence of potassium in the upper left corner of the particle (*m3*) and its association with aluminum is consistent with potassium feldspar. The titanium adduct in map *m4* is associated with sulfur (*m2*), which is also present elsewhere in the particle, and chlorine (*m5*).

Particle S2 (Fig. 3b) consists mainly of sodium and aluminum oxides (*m2* and *m3*) and carbon, perhaps as carbonate (*m1*). Smaller phases of potassium, calcium, titanium, and iron are present. What makes this particle distinctive is its shape. The nominal height of the particle is 29 μm. However, from the tilt image (*i2*), we see that much of the particle is a "finger" that extends above the rest of the particle, extending the height to 41 μm. Thus, the particle's actual shape is quite different than that shown in the normal image (*i1*). We might interpret the particle as having silicon because the right side "finger" of the particle in map *m4* exhibits silicon while the left side does not. However, it is perhaps more likely that the silicon associated with the "finger" is actually from the substrate. Here also, mapping at a lower energy would have benefitted the assessment.

Particle S3 (Fig. 3c) is quartz, based on its angularity, conchoidal fracture surface, and homogeneous SiO_2 composition. A carbon mass is attached to the lower corner of the particle. EDX at 15 keV revealed no additional elements. The tilt image (*i2*) shows the particle's thickness (approximately 2.9 μm). At 4 keV, the interaction volume for SiO_2 is within a couple hundred nanometers; thus, there is little loss of electrons to the Si wafer substrate. In this case, the particle's silicon signal in *m2* is clearly from the particle itself rather than the wafer. Nevertheless, the silicon signal is perhaps unexpectedly weak compared to the oxygen signal, since silicon is a stronger absorber of oxygen x-rays than oxygen is of silicon x-rays (mass absorption coefficients 8063 $cm^2\ g^{-1}$ vs. 1032 $cm^2\ g^{-1}$, respectively (*22*)).

Figure S8 in *Supporting Information* shows two additional particles from Seattle, S4 and S5, with similar compositions but different morphologies and distributions of elements.

3.4. Analytical Recommendations

As with all microanalysis by EDX, failure to recognize aberrations such as escape peaks and pulse pile-up (sum) peaks in EDX spectra can lead to misinterpretation of elemental maps. Nevertheless, the large variety of natural and anthropogenic particles types in the urban atmosphere, alone, presents challenges in individual particle identification. Additional challenges exist from limitations of elemental mapping with SEM for determining the spatial distribution of inhomogeneous phases. It is important to understand and adjust for potential mapping artifacts because atmospheric particles rarely offer a flat surface for x-rays to exit the particle isotropically toward the EDX detector.

As this study shows, interpretation of high-definition maps of individual particles is affected by 1) the choice of instrument parameters such as electron beam energy, 2) particle surface roughness, and 3) the complexity in the distribution of elemental phases. To avoid potential misinterpretations due to mapping artifacts, we recommend 1) imaging at different beam angles and a lower beam energy to assess particle depth and surface roughness, 2) locating the position of the x-ray detector in the map field to understand where shadow regions may exist in the particle's map, 3) redundant mapping at a lower beam energy to confine the beam interaction volume and minimize the potential x-ray contribution from the substrate, and 4) assessing relative differences in mass absorption coefficients of the particle's major elements to anticipate significant x-ray self-absorption.

This study discusses atmospheric particle heterogeneity from a strictly qualitative elemental perspective. To provide more quantitative information, semi-quantitative (standardless) EDX analysis based on beam rastering within the particle could be employed along with Monte Carlo simulations of the beam interaction volume. To identify crystalline phases in the elemental maps, electron backscatter diffraction could be employed.

To appropriately characterize aerosols in an airshed, a statistically sufficient number of particles would need to be mapped, which in all practicality, would require automation. Nevertheless, the major consideration for such an analysis is the time required. In our study, multiple-scan maps at 128x112 pixel resolution typically took around 25 min. to acquire with the Oxford Si(Li) detector. More recent use of an Oxford silicon drift EDX detector improved acquisition time by about a factor of 2. If we allow a nominal acquisition time of 10 min. for each particle, an analysis lasting 24 hours would provide maps for 144 particles at best. Thus, lengthy, yet practical, automated mapping of particles would be expected to provide high-definition maps of hundreds of particles rather than thousands.

ASSOCIATED CONTENT: *Supporting Information*

- EDX detector position and x-ray mass absorption coefficients (Fig. S1)
- Sampling and specimen preparation
- SEM Instrumentation (Fig. S2)
- Additional elemental maps and EDX spectra (Figs. S3-S8)
- Particle summary (Table S1)

ACKNOWLEDGEMENTS

The authors thank Cynthia Zeissler of NIST for a helpful review of the manuscript and Robert Willis of the U.S. EPA for helpful discussions on particle microanalysis. We thank the following people for assistance with sample collection: D. Napier, J. Brown, and E. Edgerton of Atmospheric Research and Analysis, Durham, NC; S. Biswas, B. Chakrabarti, and C. Sioutas of the Dept. of Civil and Environmental Engineering, University of Southern California, Los Angeles, CA; T. Gould of the Dept. of Civil and Environmental Engineering, University of Washington, Seattle, WA. Sample collection was funded by the U.S. EPA under Interagency Agreement DW-13-93997301-01.

Literature Cited

1. Jacobson, M. Z. Global direct radiative forcing due to multicomponent anthropogenic and natural aerosols. *Journal of Geophysical Research-Atmospheres* **2001**, *106* (D2), 1551-1568.

2. IPCC *Climate Change 2007: The Physical Science Basis*; Fourth Assessment Report of the Intergovernment Panel on Climate Change (IPCC); Cambridge University Press: New York, 2007.

3. Buseck, P. R.; Posfai, M. Airborne minerals and related aerosol particles: effects on climate and the environment. *Proceedings of the National Academy of Sciences USA* **1999**, *96* 3372-3379.

4. Ackerman, T. P.; Toon, O. P. Absorption of visible radiation in atmospheres containing mixtures of absorbing and non-absorbing particles. *Applied Optics* **1981**, *20* 3663-3998.

5. Fuller, K. A.; Malm, W. C.; Kreidenweis, S. M. Effects of mixing on extinction by carbonaceous particles. *Journal of Geophysical Research-Atmospheres* **1999**, *104* (D13), 15941-15954.

6. Kalashnikova, O. V.; Sokolik, I. N. Modeling the radiative properties of nonspherical soil-derived mineral aerosols. *Journal of Quantitative Spectroscopy and Radiative Transfer* **2004**, *87* 137-166.

7. Ebert, M.; Weinbruch, S.; Hoffman, P.; Ortner, H. M. The chemical composition and complex refractive index of rural and urban influenced aerosols determined by individual particle analysis. *Atmospheric Environment* **2004**, *38* 6531-6545.

8. Anderson, J. R.; Aggett, F. J.; Buseck, P. R.; Germani, M. S.; Shattuck, T. W. Chemistry of individual aerosol particles from Chandler, Arizona, and arid urban environment. *Environmental Science and Technology* **1988**, *22* 811-818.

9. Katrinak, K. A.; Anderson, J. R.; Buseck, P. R. Individual particle types in the aerosol of Phoenix, Arizona. *Environmental Science and Technology* **1995**, *29* 321-329.

10. Sobanska, S.; Coeur, C.; Maenhaut, W.; Adams, F. SEM-EDX Characterisation of Tropospheric Aerosols in the Negev Desert (Israel). *Journal of Atmospheric Chemistry* **2003**, *44* 299-322.

11. Krueger, B. J.; Grassian, V. H.; Cowin, J. P.; Laskin, A. Heterogeneous chemistry of individual mineral dust particles from different dust source regions: the importance of particle mineralogy. *Atmospheric Environment* **2004**, *38* 6253-6261.

12. Ro, C.; Oh, K.-Y.; Kim, H.; Chun, Y.; Osan, J.; de Hoog, J.; Van Grieken, R. Chemical speciation of individual atmospheric particle using low-A electron probe x-ray microanalysis: Characterizing "Asian Dust" deposited with rainwater in Seoul, Korea. *Atmospheric Environment* **2001**, *35* 4995-5005.

13. Artaxo, P.; Rabello, M. L. C.; Maenhaut, W.; Van Grieken, R. Trace-elements and individual particle analysis of atmospheric aerosols from the Antarctic Peninsula. *Tellus Series B-Chemical and Physical Meteorology* **1992**, *44* (4), 318-334.

14. Tegen, I.; Fung, I. Contribution to the atmospheric mineral aerosol load from land-surface modification. *Journal of Geophysical Research* **1995**, *100* (D9), 18707-18726.

15. Sokolik, I. N.; Toon, O. B. Direct radiative forcing by anthropogenic airborne mineral aerosols. *Nature* **1996**, *381* 681-683.

16. Goldstein, J. I.; Newbury, D. E.; Echlin, P.; Joy, D. C.; Lyman, C. E.; Lifshin, E.; Sawyer, L.; Michael, J. R. *Scanning Electron MIcroscopy and X-Ray Microanalysis, 3rd Edition*, 2003.

17. Fletcher, R. A., Ritchie, N. W. M., Anderson, I. M., and Small, J. A. In *Aerosol Measurement: Principles, Techniques, and Applications*, 3rd, ed.; Baron, P. A.; Willeke, K. Eds.; John Wiley & Sons, Inc.: New York, 2011;Chapter 11

18. Sokolik, I. N.; Winker, D. M.; Bergametti, G.; Gillette, D. A.; Carmichael, G.; Kaufman, Y. J.; Gomes, L.; Schuetz, L.; Penner, J. E. Introduction to special section: Outstanding problems in quantifying the radiative impacts of mineral dust. *Journal of Geophysical Research* **2001**, *106* (D16), 18015-18027.

19. Falkovich, A. H.; Ganor, E.; Levin, Z.; Formenti, P.; Rudich, Y. Chemical and mineralogical analysis of individual mineral dust particles. *Journal of Geophysical Research* **2001**, *106* (D16), 18029-18036.

20. Koren, I.; Ganor, E.; Joseph, J. H. On the relation between size and shape of desert dust aerosol. *Journal of Geophysical Research* **2001**, *106* (D16), 18047-18054.

21. McCrone, W. C. The Particle Atlas: An Encyclopedia of Techniques for Small Particle Identification. [3]. 1973.

22. Heinrich, K. F. J. In *Proceedings of the 11th International Conference on X-ray Optics and Microanalysis*, Brown, J. D.; Packwood, R. H. Eds.; University of Western Ontario: London, Ontario, 1986;

23. Wittmack, K. Brochosomes produced by leafhoppers-a widely unknown, yet highly abundant species of bioaerosols in ambient air. *Atmospheric Environment* **2005**, *39* 1173-1180.

24. Lea, F. M. *The Chemistry of Cement and Concrete*, Edward Arnold: London. 1970.

25. Iijima, A.; Sato, K.; Yano, K.; Tago, H.; Kato, M.; Kimura, H.; Furuta, N. Particle size and composition distribution analysis of automotive brake abrasion dust for the evaluation of antimony sources of airborne particulate matter. *Atmospheric Environment* **2007**, *41* 4908-4919.

FIGURE CAPTIONS

Figure 1. Electron images and elemental maps (*m*) of Atlanta particles A1-A4 (a-d, respectively). a) *i1* is 15 keV image with beam at normal; *i2* is 15 keV image with beam at 55°. Arrows indicate same feature. b) image at 15 keV with beam at normal. c) images with beam at normal. d) image at 15 keV with beam at normal. Arrows indicate brochosomes.

Figure 2. Electron images and elemental maps (*m*) of Los Angeles particles LA1-LA5 (a-e, respectively). a) *i1* is 15 keV image with beam at normal; *i2* is image with beam at 60°. The particles height is approximately 7.2 μm. b) *i1* is 15 keV image with beam at normal; *i2* is image with beam at 60°. c) *i1* is 15 keV image with beam at normal; *i2* is image with beam at 52°. d) image is at 10 keV with beam at normal. e) image is at 15 keV with beam at normal. Arrows in a-c indicated same feature in normal and tilted images.

Figure 3. Electron images and elemental maps (*m*) of Seattle particles S1-S3 (a-c, respectively). a) image is at 15 keV with beam at normal. b) *i1* is at 15 keV image with beam at normal; *i2* is image with beam at 55°. c) *i1* is 15 kev image with beam at normal; *i2* is image with beam at 52°. Arrows indicate same feature.

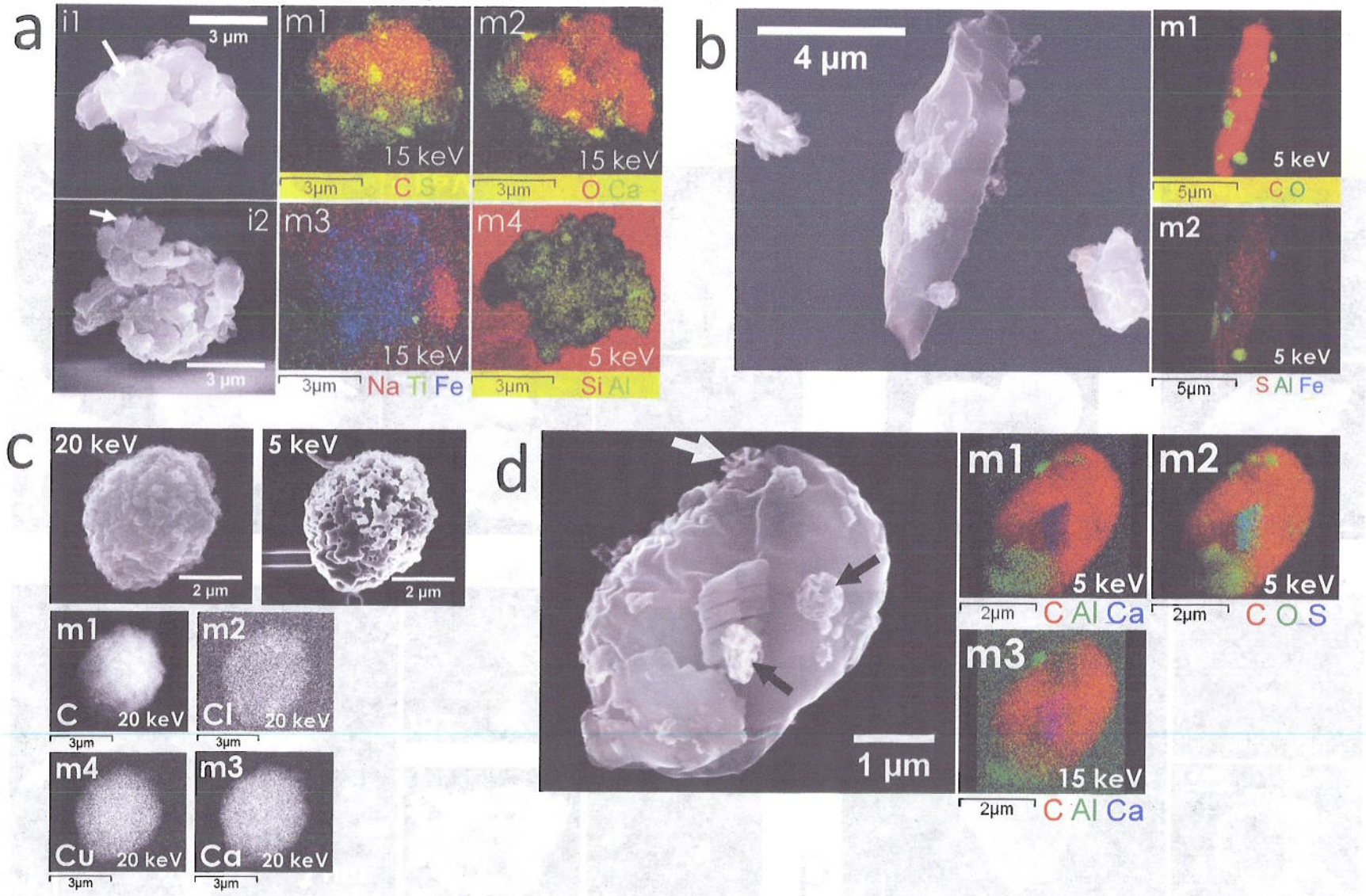

Figure 1. (Atlanta particles A1-A4)

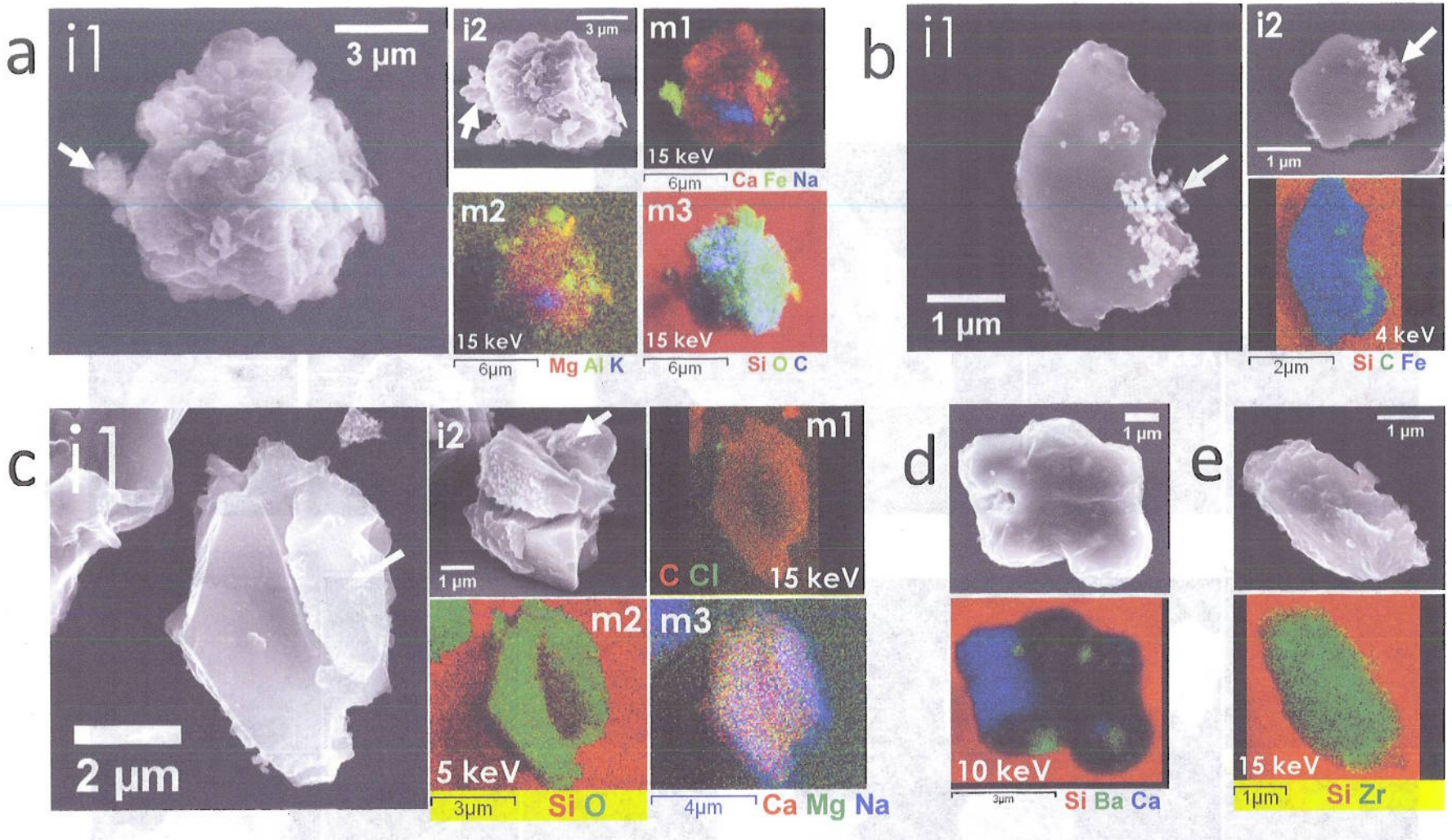

Figure 2. (Los Angeles particles LA1-LA5)

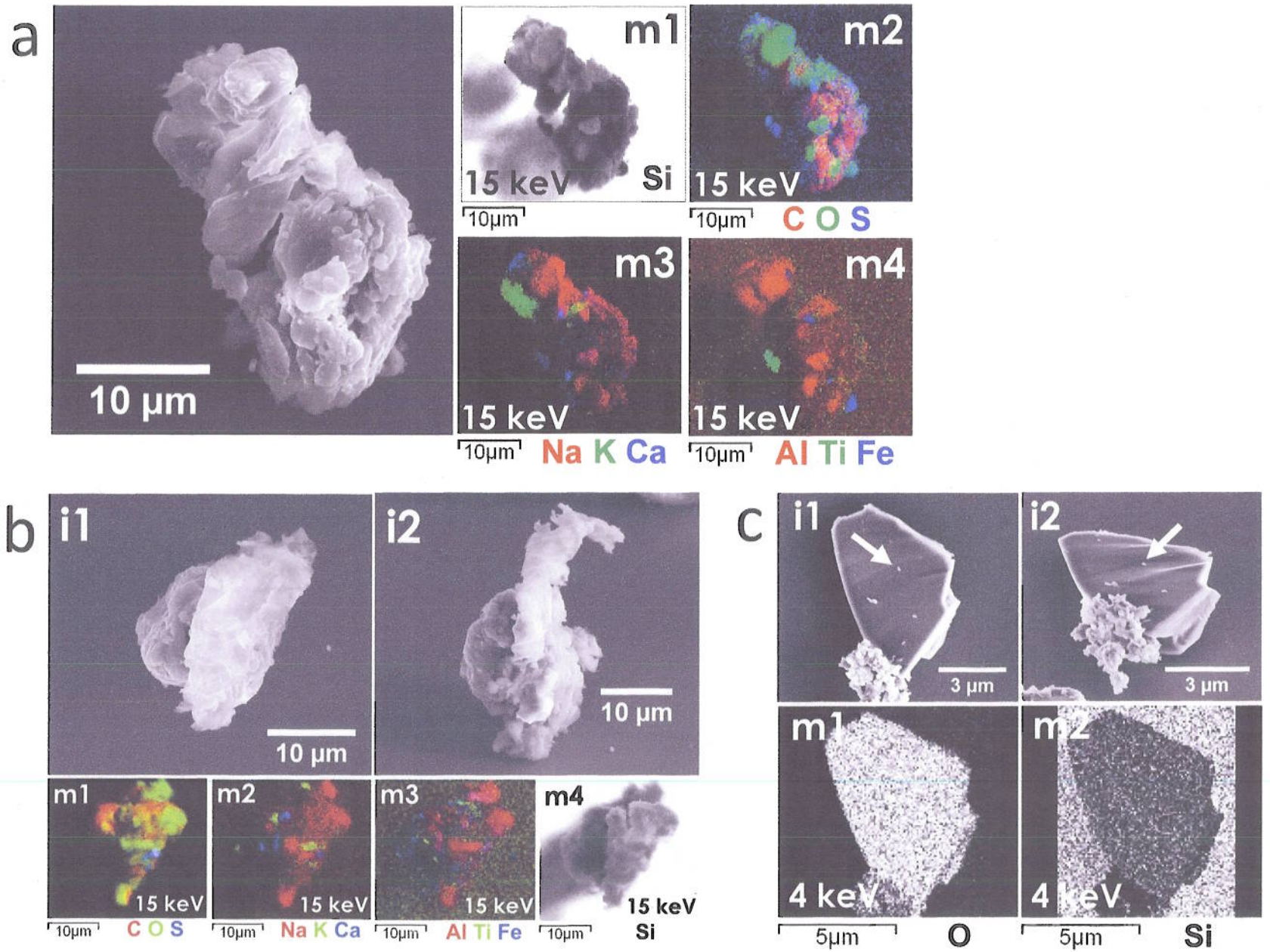

Figure 3. (Seattle particles S1-S3)

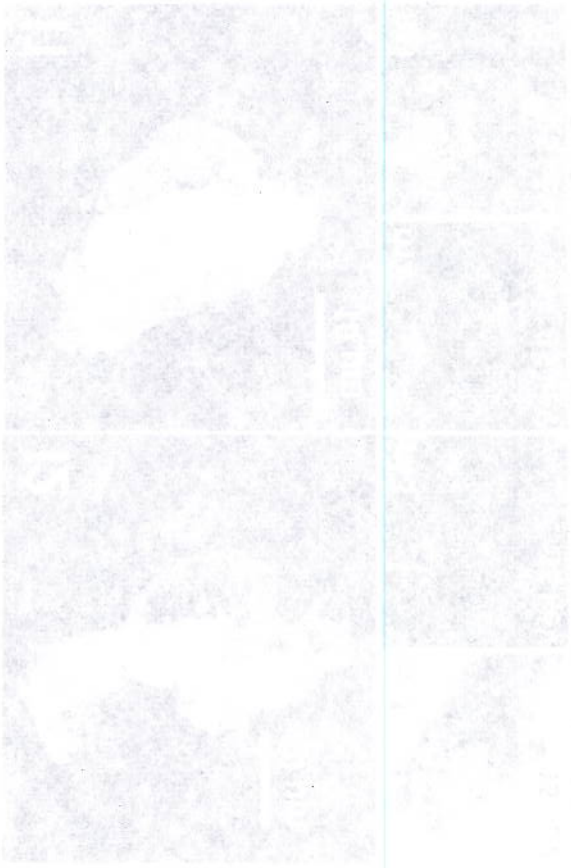

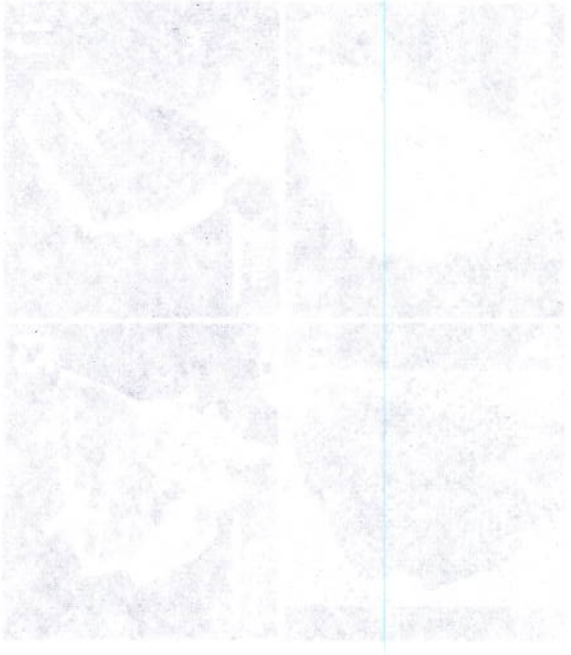

SUPPORTING INFORMATION

The Position of EDX the Detector and Differences in X-ray Mass Absorption Coefficients in Mapping

The importance of understanding how the EDX detector position impacts mapping is demonstrated by taking maps of a particle at different rotations of the microscope stage, as shown in Fig. S1. Secondary electron images of the particle with the beam at normal (a) and with the particle tilted (b), respectively, reveal the particle's surface roughness. From the silicon map (c), the shadow of the particle on the silicon substrate reveals the location of the EDX detector in the image field. From the maps (d), we see that at 0° rotation the particle's upper right corner is carbon rich while the lower left corner is aluminum rich. At 180°, the carbon rich region has shrunk, and by 270° carbon appears to be a minor component. In contrast, aluminum and calcium are not as variable with rotation. Figure S1b shows how elevated regions of the particle containing aluminum and calcium likely shielded x-rays from the low-lying carbon-rich region. Calcium and especially aluminum have much larger mass absorption coefficients for carbon x-rays (6520 $cm^2\ g^{-1}$ and 27234 $cm^2\ g^{-1}$, respectively) than carbon has for calcium $K\alpha$ and aluminum x-rays (46 $cm^2\ g^{-1}$ and 704 $cm^2\ g^{-1}$, respectively) (*1*). Thus, the aluminum and calcium phases absorbed x-rays from the carbon phase.

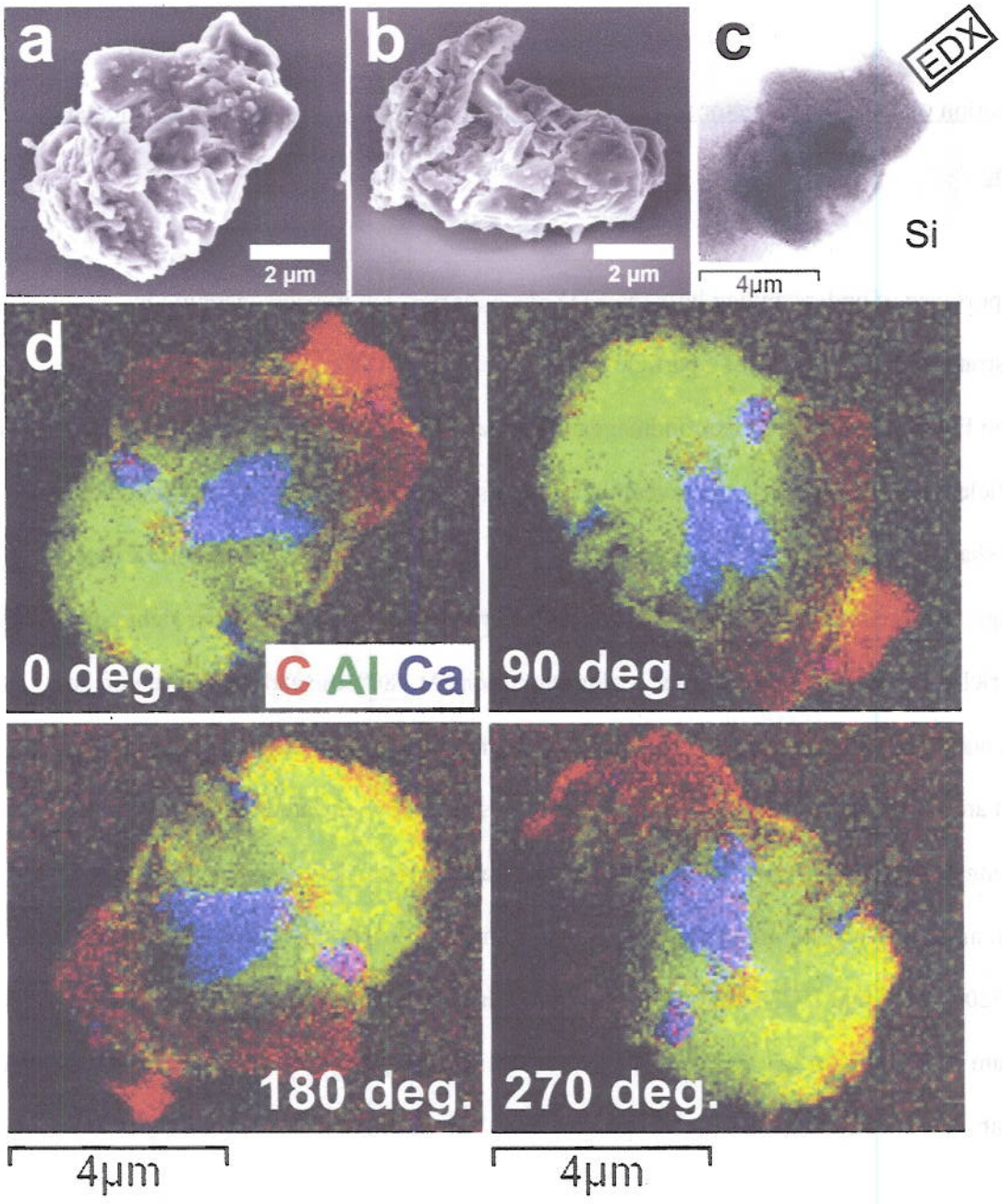

Figure S1. Coarse particle at four rotations of the microscope stage. a) and b) electron images with beam normal and with stage tilted 52° from normal, respectively. c) Elemental map showing position of EDX detector and shadow of particle on Si substrate. d) maps of carbon, aluminum, and calcium at various rotation angles of the microscope stage.

Sampling and Specimen Preparation

The Atlanta samples were collected during early September 2004 in a light industrial section of the city, approximately 4 km northwest of downtown and 2.1 km from the Interstate 75 highway. The density of buildings in the vicinity was moderately low. The virtual impactor was placed on a platform slightly above ground in a grassy corner of a relatively large urban lot, approximately 60000 m^2 (or 6 hectares). Vegetation was abundant nearby. The sampling site was operated by Atmospheric Research and Analysis and used for ongoing atmospheric sampling. On the lot, >100 m from the location of the sampler, was a maintenance building for the regional electric utility company. Truck loading and unloading activities occurred at the building as well as light industrial maintenance activities. Samples served as an example of summer aerosol from the urban southeastern U.S. and were likely influenced by vegetative emissions and secondary organic aerosols as well, perhaps, as vehicular emissions and dust from activities at the maintenance building.

The Los Angeles samples were collected in late November 2004 in a light industrial and warehousing section of the city, approximately 4 km south of downtown and approximately 150 m from the Interstate 110 highway. The density of buildings in the vicinity was moderately high. The virtual impactor was placed at ground level at the site, which also served as EPA's Los Angeles Super Site for atmospheric sampling. Particulate samples collected here were an example of autumn aerosol from the urban southwestern U.S. They were likely influenced significantly by particulate matter associated with transportation (e.g., vehicle exhaust, tire wear, brake wear, road dust).

The Seattle samples were collected in late February 2005 in a residential neighborhood approximately 9 km north of downtown and 2.9 km from the Interstate 5 highway. The virtual impactor was placed on the roof of a one-story community center adjacent to a baseball field in a neighborhood park. Buildings in the vicinity consisted mainly of single-family detached houses. The samples served as an example of winter aerosol from the urban northwestern U.S. and may have been influenced by emissions from residential woodburning in the neighborhood.

Particles were collected on quartz-fiber filters with a dichotomous high-volume virtual impactor (MSP Universal Air Sampler) operating at 300 L min^{-1} continuously for 24 h at each site. High-volume sampling on fibrous filters was employed because fibrous filters were originally used for bulk carbon analysis (*2*). The centrifugation technique for moving particles from the filters to silicon wafers squares utilized a particle transfer apparatus (*3*) that fitted inside the tube well of a microcentrifuge. Components of the apparatus were electrostatically-charged at -30 kV to create an enduringly-charged wafer surface to attract particles during centrifugation.

No substrate is ideal for x-ray microanalysis for all elements of interest in atmospheric particles (*4*). Silicon wafers are ideal for imaging; however, they are inherently problematic in detecting silicates. At higher electron beam energies the shape and porosity of most coarse-mode particles allows the beam to penetrate the particle volume, whereby silicon x-rays are detected from the wafer itself. Nevertheless, mapping at lower beam energies to better confine the electron beam within the particle, whose shape has been assessed with tilt imaging, may allow for an element that is overwhelmingly present in the substrate to be mapped from the particle itself.

SEM Instrumentation

Along with an electron beam column for conventional SEM, the FEI Nova NanoLab 600 DualBeam instrument has a focused ion beam (FIB) column that is used for nano-scale machining and fabrication as well as imaging. The two columns are offset by 52° but point to the same position on a specimen surface to allow for coordinated FIB machining/fabrication and electron-beam imaging. This functional coordination requires precisely-controlled tilting of the stage. While the ion beam was not utilized in this study, stage tilting was. When the stage is untilted, the electron beam is normal to the specimen as in conventional SEM. When the stage is tilted 52°, the ion beam enters the specimen at normal, but the electron beam enters the specimen at an oblique angle: 52° from the normal (Fig. S2). Stage tilting is adjustable up to 60°.

For determining particle height, the correction for image forshortening involves stretching the tilt image in the y-direction by 1/cosine of the angle at which imaging takes place above the substrate surface. For example, if the instrument stage is tilted 52° then the image angle above the substrate surface 90°–52°, or 38° (Fig. S2). In this case, the image is stretched by 1/cos(38°), or a factor of 1.27.

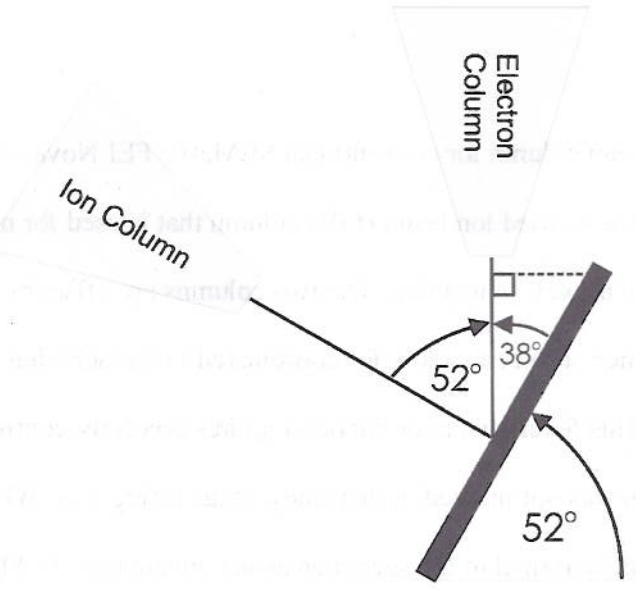

Figure S2. Schematic of the column and stage arrangement in the FIB-SEM used in this study.

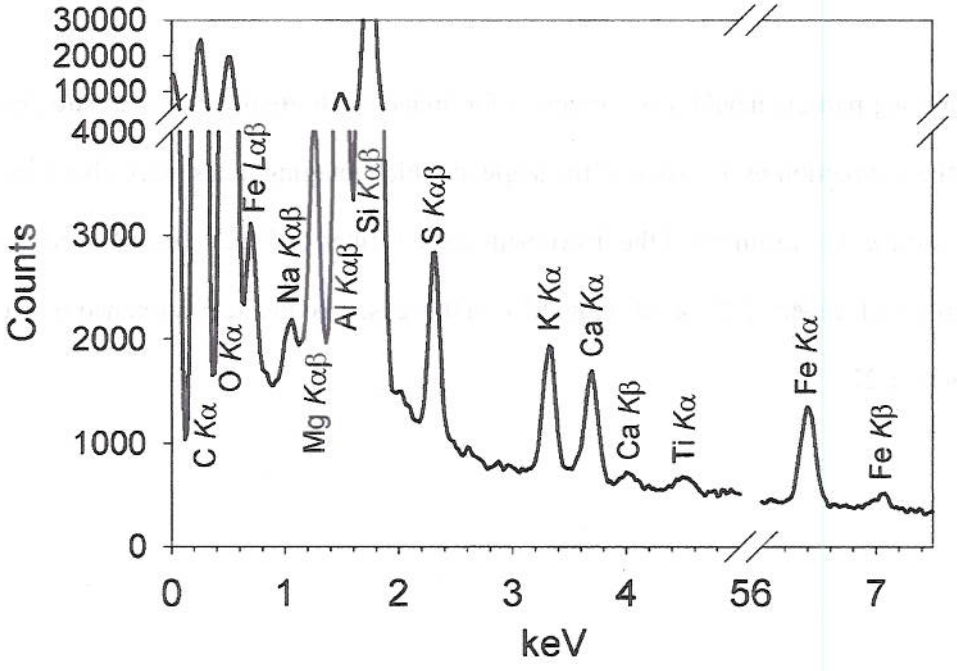

Figure S3. Within-particle EDX raster spectrum at 15 keV for Atlanta particle A1. Normalized weight percent composition from semi-quantitative analysis was 35 % carbon, 44 % oxygen, 8.1 % aluminum, 5.5 % iron, 1.9 % sulfur, 1.7 % potassium, 1.7 % calcium, 1.6 % magnesium, 0.5 % sodium, 0.3 % titanium.

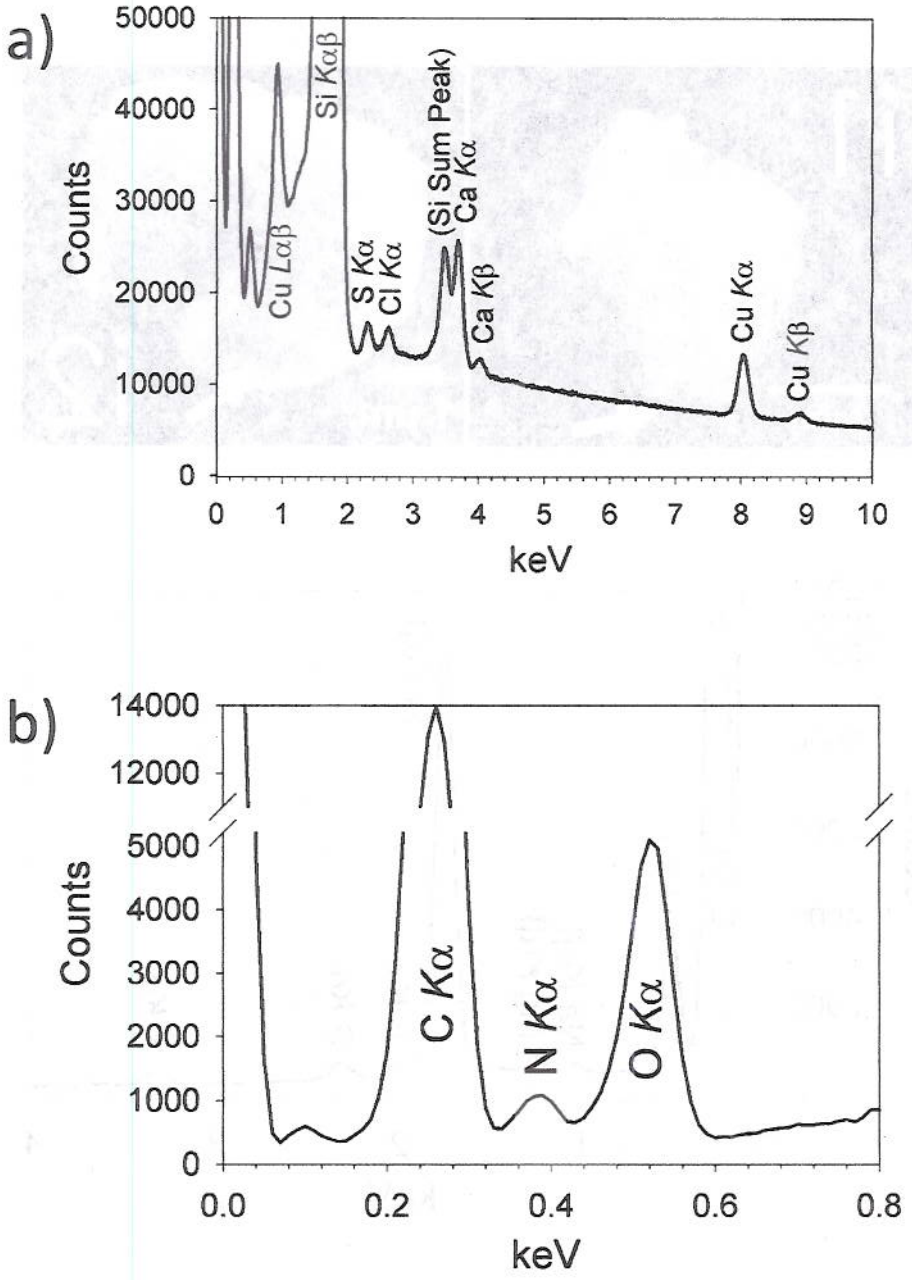

Figure S4.EDX spectra for Atlanta particle A3. a) 20 keV EDX map spectrum. b) Follow-up within-particle raster spectrum of same particle at 20 keV showing relative intensities of carbon and oxygen peaks and the presence of nitrogen.

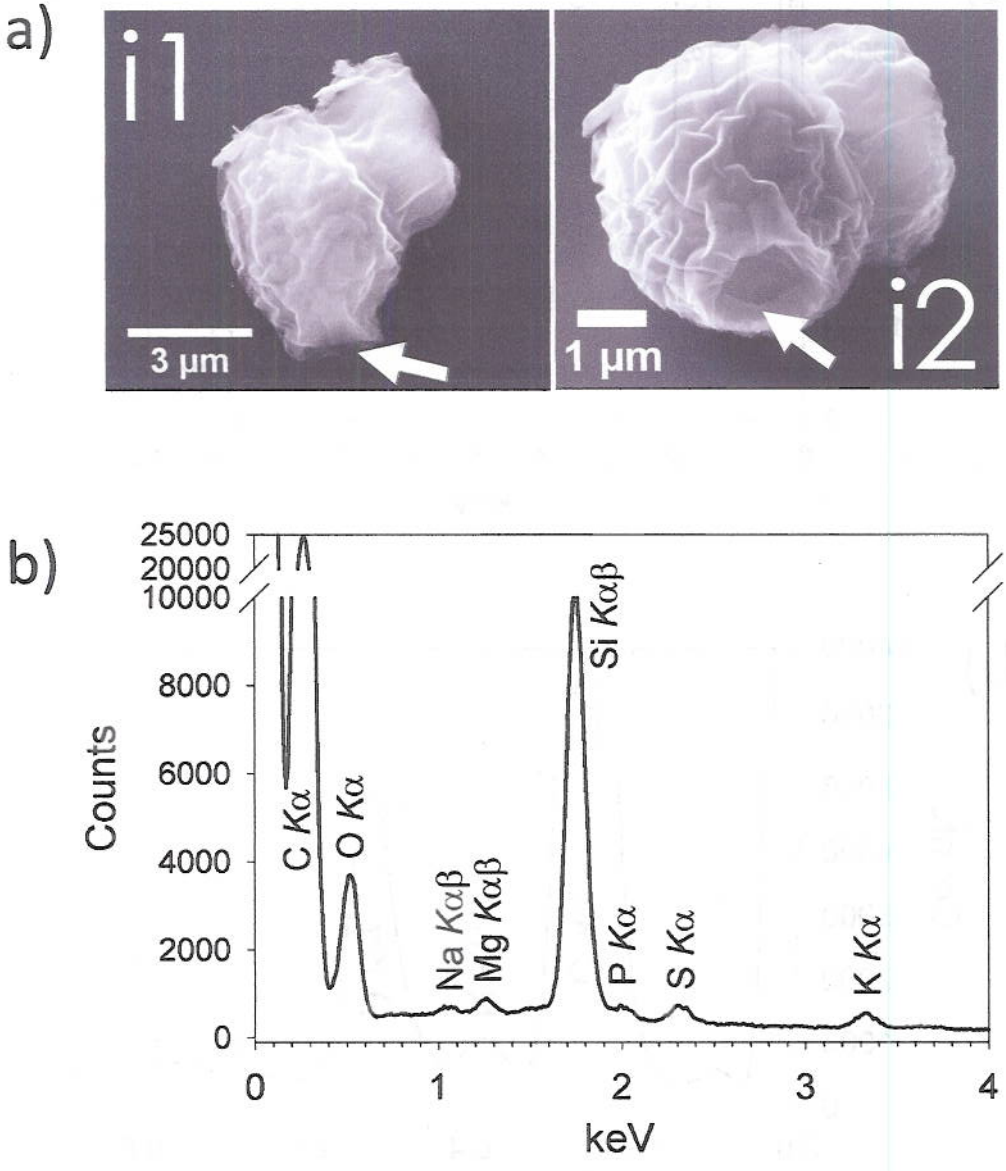

Figure S5. Biogenic Atlanta particle A5. a) normal image (*i1*) and image of tilted particle (*i2*). b) 15 keV EDX spectrum. Silicon is from the substrate. Sodium, magnesium, phosphorus, sulfur, and potassium were detected in addition to carbon and oxygen. For this particle, elemental mapping provides little benefit in determining particle origin because the particle contains nearly all carbon and has no noticeable surface adducts. The particle's identity is evident when the particle is tilted (*i2*), which reveals an attachment point to plant or animal tissue (arrow).

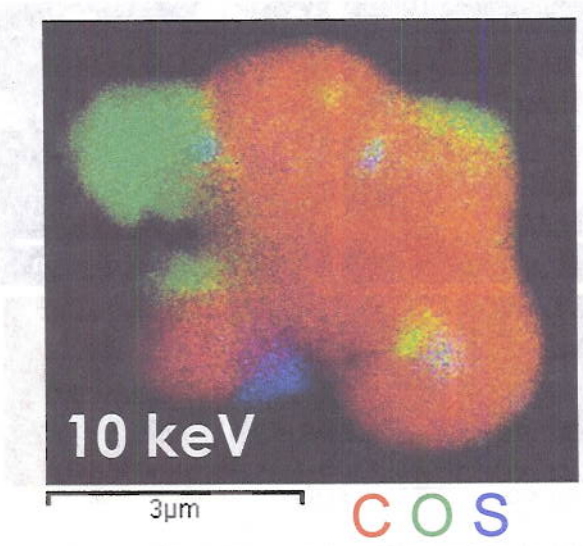

Figure S6. Carbon, oxygen, and sulfur map of Los Angeles particle A4.

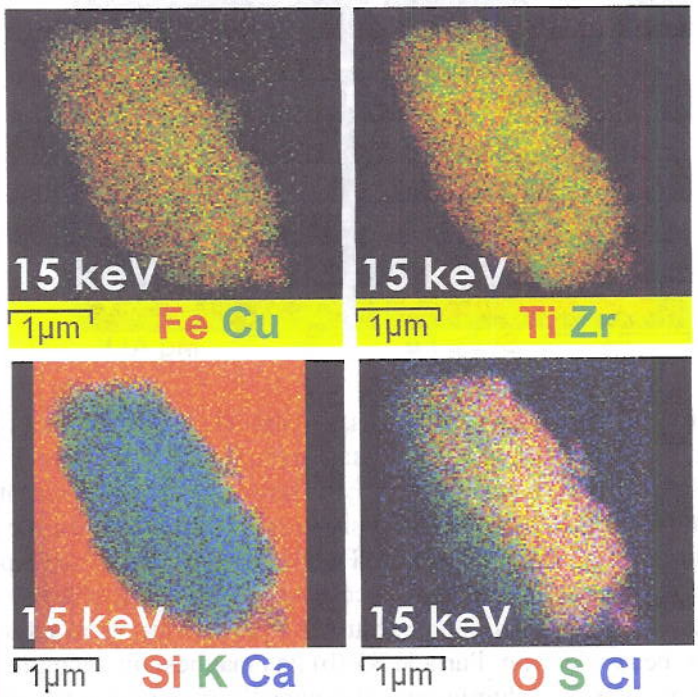

Figure S7. Maps of Los Angeles particle A5 showing iron, copper, titanium, potassium, calcium, oxygen, sulfur, and chlorine in addition to zirconium shown also in Fig. 2.

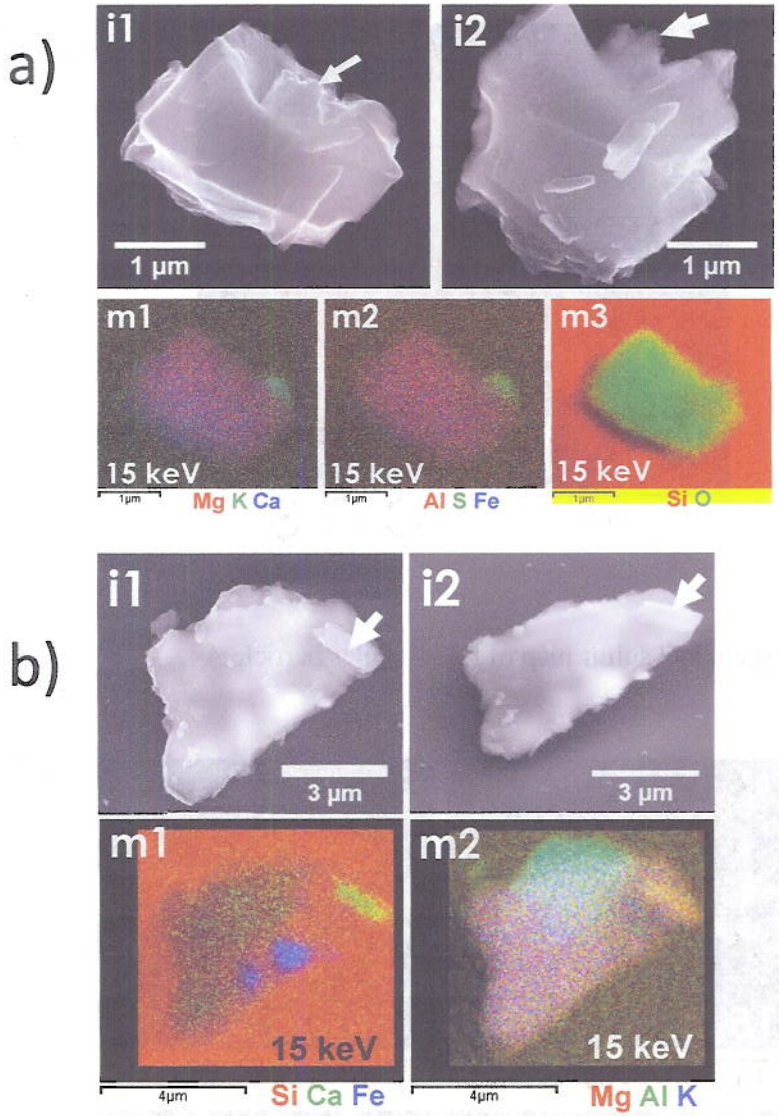

Figure S8. Comparison of two Seattle particles, S4 and S5, which have similar compositions (magnesium, calcium, aluminum, iron, and potassium), but rather different spatial distributions for the elements. Particle S4 (a) consists mainly of homogeneously-distributed magnesium, calcium, aluminum, and iron. From its composition and fracture angles, the particle resembles the mineral hornblende [e.g., $Ca_2(Fe,Mg)_4(Al,Fe)(Si_7Al)O_{22}(OH,F)_2$] with potassium as an adduct. However, the presence of silicon is inconclusive. Mapping at lower energy would likely have benefitted the assessment of silicon because the particle has substantial height (nominally 3.24 µm) to capture beam electron. Particle S5 (b) has magnesium, calcium, and potassium distributed homogeneously, but aluminum and especially iron exhibit inhomogeneities. S5 is plate-like and may be a shale fragment based on its shape (*5*). As with particle S4, the presence of silicon is inconclusive. However, because of the particle's thinness, mapping at lower energy might not help in the silicon assessment.

Particle Summary

We categorized the particles studied based on 1) the homogeneous vs. inhomogeneous distribution of elements, 2) likely origin (biogenic vs. non-biogenic/natural or non-biogenic/anthropogenic), and 3) presence surface adducts (Table S1). Among the 15 particles, 7 are non-biogenic and homogeneous, 6 are non-biogenic and inhomogeneous, and 2 are biogenic. Among the non-biogenic particles, 5 are likely natural in origin, 7 likely anthropogenic, and 1 indeterminate. Surface adducts were observed in both natural and anthropogenic particles.

While the objective of this study was not to show definitive differences in the particle populations, the few coarse particles from each site studied here suggest differences in the proportion of natural, anthropogenic, and biogenic particles from each city. More anthropogenic particles were studied from Los Angeles than from the other sites, while more biogenic particles were studied from Atlanta and more non-biogenic natural particles were studied from Seattle. The cursory observation of hundreds of additional particles from each sample substantiated the perceived differences in particle populations. For example, the summertime Atlanta sample exhibited far more biogenic particles than the Los Angeles or Seattle samples collected during fall and winter, respectively. Location also reinforced perceived differences. The prevalence of anthropogenic particles at Los Angeles is consistent with the high density of buildings near the site and the site's proximity to the downtown commercial district and a major freeway, and the prevalence of natural non-biogenic particles from Seattle is consistent with wintertime sampling in a recreational park of a residential neighborhood.

Table S1. Categories with Hypothesized Origin of Coarse Particles from Atlanta, Los Angeles, and Seattle Sampling Sites

	Categories	Subcategories		Examples	Elements Detected in Examples
1	Inhomogeneously-distributed element phases, non-biogenic	Likely natural origin		S1	C,O,Na,Al,Si,P,S,Cl,K,Ca,Ti,Fe
				S2	C,O,Na,Al,S,K,Ca,Ti,Fe
		Likely anthropogenic origin		A1	C,O,Na,Mg,Al,S,K,Ca,Ti,Fe
				LA1	C,O,Na,Mg,Al,S,K,Ca,Fe,Ti
				LA4[1]	C,O,S,Ca,Ba
		Indeterminate origin		S5	O,Mg,Al,K,Ca,Fe
2	Homogeneously-distributed element phases, non-biogenic	Likely natural origin	Without obvious surface adducts	LA3[2]	C,O,Na,Mg,S,Cl,Ca
				S4[2]	O,Mg,Al,S,K,Ca,Fe
			With obvious surface adducts	S3	(C)[3],Si,O
		Likely anthropogenic origin	Without obvious surface adducts	A3	C,O,S,Cl,Ca,Cu
				LA5	C,O,S,Cl,K,Ca,Ti,Fe,Cu,Zr[4]
			With obvious surface adducts	A2	C,(O,Al)[3],S,(Fe)[3]
				LA2	(C)[3],O,Fe
3	Biogenic	Without surface adducts		A5[5]	C, O
		With surface adducts		A4	C,(O,Al,Ca)[3]

[1] Four elements are distributed inhomogeneously; however, the main element, carbon, is distributed homogenously.
[2] Small peripheral phase present.
[3] Surface adduct composition.
[4] Zirconium exhibits some homogeneity; however, individual concentrations of zirconium indicate heterogeneity.
5 Very small amounts of sodium, magnesium, phosphorus, sulfur, and potassium were detected in EDX spectrum.

Literature Cited

1. Heinrich, K. F. J. In *Proceedings of the 11th International Conference on X-ray Optics and Microanalysis*, Brown, J. D.; Packwood, R. H. Eds.; University of Western Ontario: London, Ontario, 1986;

2. Conny, J. M.; Norris, G. A.; Gould, T. R. Factorial-based response surface modeling with confidence intervals for optimizing thermal-optical transmission analysis of atmospheric black carbon. *Analytica Chimica Acta* **2009**, *635* 144-156.

3. Conny, J. M. *Electrostatically-Assisted Centrifugation Apparatus and Related Methods,* U.S. Patent Application 12/938,636, **2010.**

4. McMurray, P. H. A review of atmospheric aerosol measurements. *Atmospheric Environment* **2000**, *34* 1959-1999.

5. McCrone, W. C. The Particle Atlas: An Encyclopedia of Techniques for Small Particle Identification. [3]. 1973.